Plasma-Based Control of Shock-Wave / Boundary-Layer Interaction

Jonathan Poggie[*]

Air Force Research Laboratory

Wright-Patterson AFB OH 45433-7512 USA

A numerical study of a Mach 14 compression ramp flow was carried out in order to determine whether a moderate power input through a glow discharge actuator located upstream of separation could lead to structural changes in the flow. First, detailed code validation was carried out by comparing computed solutions to experimental measurements of the baseline flow. Next, the effects of volumetric heating, heating at the wall, and applied body forces were considered. To avoid computational expense in this initial study, simplified models of glow discharge effects on the flow were used, rather than the detailed model used in previous studies. The most beneficial effects were obtained with surface heating and with an upstream-directed body force. With control applied, the shear layer was seen to reattach on the ramp with a slightly shallower angle, leading to reduced velocity and temperature gradients at reattachment, and consequently a reduction in the peak heat flux. The changes were confined to a narrow strip downstream of each actuator, and the integrated heat transfer rate to the entire model did not change significantly. Thus, this form of control may be useful for mitigating local hot-spots, but is probably not useful for reducing the overall heat load on this type of separated flow configuration. In future work, the full glow discharge model will be applied to this flow, with emphasis on generating an upstream body force with an applied magnetic field.

I.   Introduction

Plasma actuators are currently considered to be a promising means of flow control.[1–8] A number of different plasma generation methods have been considered for flow control schemes, including DC glow discharges, RF glow discharges, and dielectric barrier discharges, and control experiments have been carried out both with and without the presence of an applied magnetic field. Significant control effects have been observed in experiments on both high-speed[6,7] and low-speed flow.[3,4] Accurate modeling of such flow control devices, however, requires consideration of many physical phenomena, particularly space charge effects or sheaths, which are not incorporated into conventional fluid dynamics models.

Over the past few years, a prototype code (PS3D) has been written in order to model flow in the presence of finite space charge effects, and examine the plasma sheaths present near electrode surfaces.[9–18] The current version of the code is three-dimensional, and includes the effects of an applied magnetic field. Options are present in the code to model the motion of each species of charged particle with continuity/momentum equations appropriate to a low-density regime[14,16] or with a drift-diffusion equation appropriate to a high-density regime.[13,15]

In previous papers, these detailed physical models have been applied to the study of glow discharge actuators in high speed flow.[13,15,17,18] Fully-coupled, three-dimensional computations were carried out

---

[*]Research Aerospace Engineer, AFRL/VAAC, Bldg. 146 Rm. 225, 2210 Eighth St. Associate Fellow AIAA.

American Institute of Aeronautics and Astronautics Paper 2006-1007

recently, with preliminary investigations of the effect of an applied magnetic field.[17, 18] This detailed physical modeling has shown that the primary interaction of the glow discharge with the bulk gas flow is through dissipative heating, and through an electromagnetic body force if a sufficiently strong magnetic field is applied.

The present work avoids the computational cost of this high-fidelity modeling by applying a simplified plasma actuator model to the study of the control of a separated, Mach 14 compression ramp flow.[19] The object of the study is to determine whether a modest power input consisting of dissipative heating or mechanical work localized near separation can lead to structural changes in the flow. Once suitable power levels and locations are identified, further computations will be carried out using the detailed discharge model.

II.   Methods

An implicit, central-difference scheme was employed to solve the fluid conservation laws with model source terms. The physical model and numerical procedure are described in this section.

The conservation of mass, momentum, and energy for the overall gas is expressed as:

$$\frac{\partial \rho}{\partial t} + \nabla \cdot (\rho \mathbf{u}) = 0 \tag{1}$$

$$\frac{\partial}{\partial t}(\rho \mathbf{u}) + \nabla \cdot (\rho \mathbf{uu} - \mathbf{\Sigma}) = \mathbf{f} \tag{2}$$

$$\frac{\partial \mathcal{E}}{\partial t} + \nabla \cdot (\mathbf{u}\mathcal{E} - \mathbf{\Sigma} \cdot \mathbf{u} + \mathbf{Q}) = \mathbf{f} \cdot \mathbf{u} + S \tag{3}$$

where ρ is the gas density, $\mathbf{u}$ is its velocity, $\mathbf{\Sigma}$ is the total stress tensor, $\mathcal{E} = \rho(\epsilon + u^2/2)$ is the total fluid energy, ϵ is the internal energy, and $\mathbf{Q}$ is the heat flux. The source terms on the right hand sides of the conservation equations include a body force $\mathbf{f}$ and a dissipative energy source S.

The total stress tensor $\mathbf{\Sigma}$ is given by the usual constitutive equation for a Newtonian fluid and the heat flux $\mathbf{Q}$ follows Fourier's heat conduction law:

$$\Sigma_{ij} = -p\delta_{ij} + \mu \left(\frac{\partial u_i}{\partial x_j} + \frac{\partial u_j}{\partial x_i} \right) - \frac{2}{3}\mu \frac{\partial u_k}{\partial x_k}\delta_{ij} \tag{4}$$

$$Q_i = -k\frac{\partial T}{\partial x_i} \tag{5}$$

where p is the pressure, μ is the viscosity, and k is the thermal conductivity. The transport coefficients were evaluated using the correlations given in Ref. 20. The working fluid (air) was assumed to be a calorically and thermally perfect gas: $\epsilon = c_v T$ and $p = \rho R T$, where T is the temperature, c_v is the specific heat, and R is the ideal gas constant.

Phenomenological models of dissipative heating and body forces were considered, and their effects on the flow were evaluated. The volumetric heating model had the form:

$$S = \frac{Q}{\pi^{3/2}a^3} \exp\left(-\frac{r^2}{a^2}\right) \tag{6}$$

and was added to the total energy equation. Note that $\int_0^\infty S4\pi r^2 dr = Q$. The variable r represents the distance from the center (x_c, y_x, z_c) of the heating: $r = \sqrt{(x - x_c)^2 + (y - y_c)^2 + (z - z_c)^2}$. The applied body force had the analogous form:

$$\mathbf{f} = \frac{2Q}{U_\infty \pi^{3/2}a^3} \exp\left(-\frac{r^2}{a^2}\right) \mathbf{e}_x \tag{7}$$

and was added to the momentum equations, with $\mathbf{f} \cdot \mathbf{u}$ added to the total energy equation. Note that $\frac{1}{2}U_\infty \int_0^\infty f_x 4\pi r^2 dr = Q$, so that the net mechanical power delivered to the fluid is about the same as the heating specified in Eq. (6). The surface heating model had the form:

$$q_w = \frac{Q}{\pi a^2} \exp\left(-\frac{r^2}{a^2}\right) \tag{8}$$

and was applied as a boundary condition. Note that $\int_0^\infty q_w 2\pi r dr = Q$. The variable r represents the distance along the wall ($y = 0$) from the center of the heating: $r = \sqrt{(x - x_c)^2 + (z - z_c)^2}$.

The conservation laws were solved using an approximately-factored, implicit scheme, related to those developed by Beam and Warming[21] and Pulliam.[22] Applying the standard transformation from physical coordinates (x, y, z) to grid coordinates (ξ, η, ζ), the conservation equations (1)–(3) can be written in the form:

$$\frac{\partial \overline{U}}{\partial t} + \frac{\partial \overline{E}}{\partial \xi} + \frac{\partial \overline{F}}{\partial \eta} + \frac{\partial \overline{G}}{\partial \zeta} = \frac{\partial \overline{E}_v}{\partial \xi} + \frac{\partial \overline{F}_v}{\partial \eta} + \frac{\partial \overline{G}_v}{\partial \zeta} + \overline{S} \tag{9}$$

where the usual notation[23] is used: U is the the vector of dependent variables, E is a flux, $\overline{U} = U/J$, $\overline{E} = (\xi_x E + \xi_y F + \xi_z G)/J$, etc.

Writing Eq. (9) as $\partial \overline{U}/\partial t = R$, and discretizing in time, we have:

$$(1 + \theta)\overline{U}^{n+1} - (1 + 2\theta)\overline{U}^n + \theta\overline{U}^{n-1} = \Delta t R^{n+1} \tag{10}$$

where $\theta = 0$ for an implicit Euler scheme and $\theta = 1/2$ for a three point backward scheme. We introduce subiterations such that $\overline{U}^{n+1} \to \overline{U}^{p+1}$, with $\Delta\overline{U} = \overline{U}^{p+1} - \overline{U}^p$. The right hand side R^{n+1} is linearized in the standard 'thin layer' manner. Collecting the implicit terms on the left hand side, and introducing approximate factoring and a subiteration time step $\Delta\hat{t}$ gives:

$$\begin{aligned}
&\left[I - \frac{\Delta\hat{t}}{1 + \theta}(B + \delta_\xi A_1 + \delta_\xi R_1 \delta_\xi + D_{i\xi})\right] \times \\
&\left[I - \frac{\Delta\hat{t}}{1 + \theta}(\delta_\eta A_2 + \delta_\eta R_2 \delta_\eta + D_{i\eta})\right] \times \\
&\left[I - \frac{\Delta\hat{t}}{1 + \theta}(\delta_\zeta A_3 + \delta_\zeta R_3 \delta_\zeta + D_{i\zeta})\right] \Delta\overline{U} = \\
&-\frac{\Delta\hat{t}}{1 + \theta}\left\{\frac{(1 + \theta)\overline{U}^p - (1 + 2\theta)\overline{U}^n + \theta\overline{U}^{n-1}}{\Delta t} - R^p - D_e\overline{U}^p\right\}
\end{aligned} \tag{11}$$

where B is the source Jacobian, and A_{1-3} and R_{1-3} are flux Jacobians. The spatial derivatives are evaluated using second order central differences.

The symbols D_i and D_e are, respectively, the implicit and explicit damping operators described by Pulliam.[22] The explicit damping operator uses a nonlinear blend of second- and fourth-order damping.[24]

In the implementation of the computer code, multi-level parallelism is exploited by using vectorization, multi-threading with OpenMP commands,[25] and multi-block decomposition implemented through MPI commands.[26] Further, the code is set up to run in either a time-accurate mode, or with local time stepping to accelerate convergence.

It was found to be efficient in many cases to compute an initial solution using a low-storage fourth-order Runge-Kutta time-integration method (e.g., see Sec. 6.6.8 of Ref. 23) and local time-stepping, and then to compute the final solution using the implicit method with a global time-step.

III. Results

Two- and three-dimensional calculations were carried out for a series of Mach 14 compression ramp flows originally studied by Holden and Moselle.[19] The ramp configuration consists of an initial flat plate of length $L = 0.439$ m and width $W = 0.610$ m mounted parallel to the freestream, followed by a second plate, inclined to the freestream by an angle θ. The flow conditions are listed in Table 1.

This flow has been used as a benchmark case in a number of previous computational studies.[27–32] Magnetohydrodynamic flow control studies were carried out by Updike et al.,[32] who demonstrated that a relatively large-scale MHD device applied at the corner could eliminate separation completely if a sufficiently strong accelerating force were applied. The present study focuses, in contrast, on a more localized glow discharge-based control with much lower input power levels.

Parameter	value
M	14.1
Re_L	1.04×10^5
T_w/T_∞	4.1
W/L	1.39
θ	15°, 18°, 24°

Table 1. Flow conditions for the Holden-Moselle[19] experiments.

A. Validation and Baseline Flow Structure

An initial set of two-dimensional calculations was carried out for each of three ramp angles (15°, 18°, and 24°) on a relatively coarse grid ($202 \times 60 \times 5$) and on a finer grid ($404 \times 120 \times 5$). Uniformity was imposed along the z-direction in all the two-dimensional calculations.

Figure 1 shows the flow field predicted on the fine grid for each case. The pressure fields are shown in Figs. 1a, 1c, and 1e for the 15°, 18°, and 24° cases, respectively. A close-up view of each of the corresponding temperature fields is shown with selected streamlines in Figs. 1b, 1d, and 1f. In each case, a weak shock is seen emanating from the plate leading edge, generated by the hypersonic boundary layer displacement effect. A strong oblique shock, due to the turning angle θ of the ramp is seen farther downstream. In the intermediate region near the corner, the 15° case displays incipient separation (Fig. 1b), the 18° case has a very small small separated zone (Fig. 1d), and the 24° case has a large recirculating zone (Fig. 1f). A shock / compression-wave system appears with flow separation, and these waves interact with the leading edge shock and ramp shock in a complex manner near reattachment. (Hung and MacCormack[27] have identified this as an Edney[33] Type VI interaction.) There is a striking thinning of the boundary layer in this region, often called the 'neck'.[27] Farther downstream, the boundary layer displays non-monotonic density and temperature profiles, reflecting the embedded shear layer generated by the shock intersection near the neck.

Figure 2 shows profiles of the properties along the wall for each computational case, along with the experimental measurements of Holden and Moselle. The pressure coefficient is defined as $C_p = 2(p_w - p_\infty)/(\rho_\infty U_\infty^2)$, the heat transfer coefficient as $C_h = q_w/[\rho_\infty U_\infty(H_\infty - H_w)]$, and the skin friction coefficient as $C_f = 2\tau_w/(\rho_\infty U_\infty^2)$, where H is the total enthalpy and the subscripts ∞ and w indicate that the quantity is evaluated in the freestream or wall, respectively. Overall, the trends are similar to those observed in previous two-dimensional calculations.[27–32] The pressure and heat transfer coefficients tend to be over-predicted near reattachment in all cases. Separation and reattachment locations are predicted adequately for the 15° and 18° cases, but separation occurs too early in the 24° case on the finer grid, possibly because of the inherent three-dimensionality of this flow.

Note that the pressure overshoot (peak greater than the inviscid pressure rise corresponding to the flow turning angle θ) increases with increasing ramp angle (Figs. 2a, 2d, and 2g). Similar trends are seen in heat transfer and skin friction. These trends indicate the increasing strength of the interaction at reattachment with increasing ramp angle.

To examine the issue of spanwise nonuniformity in the 24° case, three-dimensional calculations were carried out on $202 \times 60 \times 60$ and $404 \times 120 \times 120$ grids. The results are summarized in Fig. 3. A diagram of the wall boundary conditions is shown in Fig. 3a. To allow for the finite width of the plate, a portion of the bottom of the computational domain was assigned a no-slip boundary condition to represent the plate and ramp. Near the spanwise boundaries, either slip or outflow boundary conditions were used, as indicated in the figure.

A contour plot of the magnitude of the skin friction and trajectories of the skin friction vector field $\tau \cdot \mathbf{n}$, where τ is the shear stress tensor and $\mathbf{n}$ is the wall-normal unit vector, are shown in Fig. 3b. Note that the degree of spanwise nonuniformity in this solution is less than that observed by Rudy $et\ al.$,[30] who used a coarser grid and slightly different boundary conditions. Temperature contours are shown in Fig. 3c, along with ribbons of streamlines originating in the recirculating zone in the centerplane. These ribbons illustrate the three-dimensional, spiraling flow near the ramp corner.

Centerline profiles are compared to the experimental measurements in Figs. 3d-f. The results are qualitatively similar to the results of the corresponding two-dimensional calculations shown in Figs. 2g-i, except that the size of the separated zone is much more accurately predicted by the three-dimensional computations.

B.   Effects of heating and body force

With the ability of the code to simulate the baseline flow validated, a series of exploratory studies of the effect of volumetric heating (Eq. 6), body forces (Eq. 7), and surface heating (Eq. 8) were carried out. All the computations were three-dimensional, and carried out on a $202 \times 60 \times 60$ grid. The following baseline values were used in each case: $Q = 100$ W, $x_c = L/2 = 0.220$ m, $y_c = 0.008$ m (or zero for surface heating), $z_c = 0$ m, and $a = 0.005$ m.

Figure 4 shows the effects of heat addition on the surface properties at the centerline. Three cases are shown: the baseline flow, volumetric heat addition (Eq. 6), and surface heat addition (Eq. 8).

Overall, the surface heating had the greatest effect, perhaps because the added energy remained localized near the wall. The pressure peak near reattachment was somewhat broadened and reduced with the presence of heating (Fig. 4a). Because of the varying wall and total temperatures, a modified heat transfer coefficient $C_h = q_w/[\rho_\infty U_\infty H_\infty]$ is shown in Fig. 4b. Heat transfer to the plate is increased just downstream of the 'actuator' location, but is decreased at reattachment. The skin friction distribution shows similar behavior, and indicates that both separation and reattachment are shifted slightly downstream with heating.

To illustrate the reasons for the reduction in reattachment heat transfer and skin friction with heating, Figs. 4d-f show boundary layer profiles near separation and reattachment, as well as a portion of the density field near reattachment. Heating is seen to produce slightly fuller velocity profiles upstream of separation. This difference produces a subtle change in the angle at which the shear layer contacts the ramp (Fig. 4f), leading to reduced wall-normal derivatives of velocity and temperature (Fig. 4e), and thus reduced fluxes at the wall near reattachment.

Analogous plots for the effect of an applied body force are shown in Fig. 5. Three cases are shown: the baseline case, a case with an applied force as in Eq. (7), and an analogous case with a negative (upstream) body force.

The downstream directed force is seen to have a slightly deleterious effect on the flow. Both heat transfer (Fig. 5b) and skin friction (Fig. 5c) increase somewhat near reattachment. The size of the separation bubble is decreased because of the acceleration of the near-wall portion of the boundary layer by the body force (Fig. 5d), and greater wall-normal derivatives occur near reattachment (Fig. 5e).

In contrast, an upstream body force has a strikingly beneficial effect. This is a somewhat surprising result, given that such a force would be expected to, and indeed does, slow the flow and promote separation,

as illustrated in the larger separated zone seen in the skin friction plot of Fig. 5c. The result seems to be analogous to that observed with heating: a small alteration in the angle at which the shear layer impinges on the ramp can lead to a significant decrease in the strength of the interaction at reattachment (Fig. 5f).

Additional cases were considered with multiple control elements. The effects of each control case on the peak heating at reattachment are summarized in Table 2. It is seen that all the control cases, except the downstream directed force, significantly reduce the peak heat transfer rate.

Case	x/L	C_f	$C_h = \frac{q_w}{\rho_\infty U_\infty H_\infty}$	C_p
Baseline	1.28	2.25×10^{-2}	2.05×10^{-2}	0.741
Surface Heating	1.30	1.58×10^{-2}	1.73×10^{-2}	0.668
Surface Heating x 5	1.32	1.77×10^{-2}	1.80×10^{-2}	0.731
Volumetric Heating	1.29	1.86×10^{-2}	1.90×10^{-2}	0.707
Volumetric Heating x 5	1.30	1.97×10^{-2}	1.91×10^{-2}	0.741
Downstream force	1.27	2.59×10^{-2}	2.19×10^{-2}	0.731
DS Force & Vol. Heating (50 W each)	1.28	2.15×10^{-2}	2.03×10^{-2}	0.722
Upstream Force	1.30	1.83×10^{-2}	1.86×10^{-2}	0.723

Table 2. Conditions at peak reattachment heating ($z/L = 0$): effect of control.

The control effects described above tended to be confined to a strip downstream with a characteristic width of the same order as that of the control actuator. Figure 6 shows skin friction lines (trajectories of the wall shear stress vector field) and heat transfer coefficient for surface heating cases with one and with five actuators. Control is seen to introduce a significant degree of spanwise nonuniformity. For the spacing considered here, multiple actuators did not seem to interfere with each other.

The heat transfer integrated over the surface $q_{\text{net}} = \iint \mathbf{q}_w \cdot \mathbf{n} \, dS$ was computed to determine the net effect of each control case. The results are shown in Table 3. (Note that the reductions in heating to the flat plate portion of the model for the surface heating cases are somewhat misleading because the domain of integration includes a region of opposite sign at the actuators.) Although significant local decreases in heat transfer have occurred (see Table 2 and Fig. 6), the net heat load is seen to remain nearly the same. Close inspection of Fig. 6 indicates that the heat transfer is strongly reduced directly downstream of each actuator near the reattachment hot spot, but outboard of that region the heat transfer is moderately increased over a large area. Thus, this form of control may be useful for mitigating local hot-spots, but appears to have a negligible effect on the net heat transfer.

Case	Total	Flat Plate	Ramp
Baseline	17.1 kW	2.7 kW	14.5 kW
Surface Heating	-0.2 %	-1.0 %	-0.1 %
Surface Heating x 5	-1.1 %	-7.1 %	0.0 %
Volumetric Heating	$+0.1$ %	$+0.9$ %	0.0 %
Volumetric Heating x 5	$+1.1$ %	$+7.2$ %	0.0 %
Downstream Force	$+0.3$ %	$+0.8$ %	$+0.2$ %
DS Force & Vol. Heating (50 W each)	$+0.2$ %	$+0.8$ %	$+0.1$ %
Upstream Force	-0.3 %	-0.4 %	-0.2 %

Table 3. Effect of control on net (integrated) surface heat transfer.

IV.   Summary and Conclusions

Over the past several years, a program has been underway to develop a capability to numerically simulate experiments with plasma actuators and evaluate their potential for flow control applications. Toward this end, a three-dimensional computer code has been written to provide detailed physical modeling of plasma actuator behavior. In recent work, fully-coupled, three-dimensional calculations of a DC discharge in a hypersonic crossflow have been carried out. This detailed physical modeling has shown that the primary interaction of the glow discharge with the bulk gas flow is through dissipative heating, and through an electromagnetic body force if a sufficiently strong magnetic field is applied.

The present work has avoided the computational cost of high-fidelity modeling by applying a simplified plasma actuator model to the study of the control of a separated compression ramp flow. The object of the study was to determine whether a modest power input consisting of dissipative heating or mechanical work can lead to structural changes in the flow if localized to a sensitive region of the flow near separation.

The computer code was first validated against experiment for three Mach 14 compression ramp flows originally studied by Holden and Moselle,[19] who measured wall pressure, heat transfer, and skin friction on the model centerline. Two-dimensional calculations were carried out first. Adequate comparison with experiment was obtained for the 15° and 18° ramp cases, but the streamwise extent of the separated region was too large for the 24° case. This latter case was re-examined with three-dimensional calculations, and much better agreement with experiment was obtained.

Three-dimensional calculations of the 24° ramp case were then carried out for different model control actuators. The effects of volumetric heating, heating at the wall, a downstream body force, an upstream body force, and combined cases were considered. In each case a total input power of 100 W was applied to each actuator, mounted halfway down the initial flat plate.

The most beneficial effects were obtained with surface heating and with an upstream-directed body force, which caused the shear layer to reattach on the ramp with a slightly shallower angle, leading to reduced velocity and temperature gradients at reattachment. The changes were confined to a narrow strip downstream of each actuator, and the integrated heat transfer rate to the entire model did not change significantly. Thus, this form of control may be useful for mitigating local hot-spots, but is probably not useful for reducing the overall heat load on such a separated flow configuration.

In future work, the full glow discharge model[18] will be applied to this flow, with emphasis on generating an upstream body force with an applied magnetic field.

Acknowledgments

References

[1]Bychkov, V., Kuz'min, G., Minaev, I., Rukhadze, A., and Timofeev, I., "Sliding Discharge Application in Aerodynamics," AIAA Paper 2003-0530, American Institute of Aeronautics and Astronautics, Reston VA, January 2003.

[2]Enloe, C. L., McLaughlin, T. E., VanDyken, R. D., Kachner, K. D., Jumper, E. J., and Corke, T. C., "Mechanisms and Responses of a Single Dielectric Barrier Plasma," AIAA Paper 2003-1021, American Institute of Aeronautics and Astronautics, Reston VA, January 2003.

[3]Post, M. L. and Corke, T. C., "Separation Control on High Angle of Attack Airfoil Using Plasma Actuators," AIAA Paper 2003-1024, American Institute of Aeronautics and Astronautics, Reston VA, January 2003.

[4]Roth, J. R., Sin, H., Madhan, R. C. M., and Wilkinson, S. P., "Flow Re-attachment and Acceleration by Paraelectric and

Peristaltic Electrohydrodynamic (EHD) Effects," AIAA Paper 2003-0531, American Institute of Aeronautics and Astronautics, Reston VA, January 2003.

[5]Wilkinson, S. P., "Investigation of an Oscillating Surface Plasma for Turbulent Drag Reduction," AIAA Paper 2003-1023, American Institute of Aeronautics and Astronautics, Reston VA, January 2003.

[6]Kimmel, R. L., Hayes, J. R., Menart, J. A., and Shang, J., "Effect of Surface Plasma Discharges on Boundary Layers at Mach 5," AIAA Paper 2004-0509, American Institute of Aeronautics and Astronautics, Reston, VA, January 2004.

[7]Meyer, R., Chintala, N., Bystricky, B., Hicks, A., Cundy, M., Lempert, W. R., and Adamovich, I. V., "Lorentz Force Effect on a Supersonic Ionized Boundary Layer," AIAA Paper 2004-0510, American Institute of Aeronautics and Astronautics, Reston, VA, January 2004.

[8]Wie, D. M. V., Risha, D. J., and Suchomel, C. F., "Research Issues Resulting from an Assessment of Technologies for Future Hypersonic Aerospace Systems," AIAA Paper 2004-1357, American Institute of Aeronautics and Astronautics, Reston, VA, January 2004.

[9]Poggie, J. and Gaitonde, D. V., "Electrode Boundary Conditions in Magnetogasdynamic Flow Control," AIAA Paper 2002-0199, American Institute of Aeronautics and Astronautics, Reston VA, January 2002.

[10]Poggie, J., Gaitonde, D. V., and Sternberg, N., "Numerical Simulation of Plasma Sheaths in Aerodynamic Applications," AIAA Paper 2002-2166, American Institute of Aeronautics and Astronautics, Reston VA, May 2002.

[11]Poggie, J., "Numerical Simulation of Electromagnetic Flow Control for Hypersonic Systems," AIAA Paper 2002-5182, American Institute of Aeronautics and Astronautics, Reston VA, October 2002.

[12]Poggie, J. and Sternberg, N., "Numerical Simulation of Electrode Sheaths in a Magnetized Plasma," AIAA Paper 2003-0359, American Institute of Aeronautics and Astronautics, Reston VA, January 2003.

[13]Poggie, J. and Sternberg, N., "Numerical Simulation of Glow Discharges for High-Speed Flow Control," AIAA Paper 2004-0177, American Institute of Aeronautics and Astronautics, Reston VA, January 2004.

[14]Sternberg, N. and Poggie, J., "Plasma-Sheath Transition in the Magnetized Plasma-Wall Problem for Collisionless Ions," *IEEE Transactions on Plasma Science*, Vol. 32, No. 6, 2004, pp. 2217–2226.

[15]Poggie, J., "Numerical Exploration of Flow Control with Glow Discharges," AIAA Paper 2004-2658, American Institute of Aeronautics and Astronautics, Reston VA, June 2004.

[16]Poggie, J. and Sternberg, N., "Transition from the Constant Ion Mobility Regime to the Ion-Atom Charge-Exchange Regime for Bounded Collisional Plasmas," *Physics of Plasmas*, Vol. 12, No. 2, Feb. 2005.

[17]Poggie, J., "Computational Studies of High-Speed Flow Control with Weakly-Ionized Plasma," AIAA Paper 2005-0784, American Institute of Aeronautics and Astronautics, Reston VA, January 2005.

[18]Poggie, J., "DC Glow Discharges: A Computational Study for Flow Control Applications," AIAA Paper 2005-5303, American Institute of Aeronautics and Astronautics, Reston VA, June 2005.

[19]Holden, M. S. and Moselle, J. R., "Theoretical and Experimental Studies of the Shock Wave - Boundary Layer Interaction on Compression Surfaces in Hypersonic Flow," Tech. Rep. ARL 70-0002, Aerospace Research Laboratories, January 1970.

[20]White, F. M., *Viscous Fluid Flow*, McGraw-Hill, New York, 2nd ed., 1991.

[21]Beam, R. and Warming, R., "An Implicit Factored Scheme for the Compressible Navier-Stokes Equations," *AIAA Journal*, Vol. 16, No. 4, 1978, pp. 393–402.

[22]Pulliam, T. H., "Implicit Finite-Difference Simulations of Three-Dimensional Compressible Flow," *AIAA Journal*, Vol. 18, No. 2, 1980, pp. 159–167.

[23]Hoffmann, K. A. and Chiang, S. T., *Computational Fluid Dynamics*, Engineering Educational System, Wichita KS, 4th ed., 2000, 2 vols.

[24]Jameson, A., Schmidt, W., and Turkel, E., "Numerical Solutions of the Euler Equations by a Finite Volume Method Using Runge-Kutta Time Stepping Schemes," AIAA Paper 81-1259, American Institute of Aeronautics and Astronautics, Reston, VA, 1981.

[25]Chandra, R., Dagum, L., Kohr, D., Maydan, D., McDonald, J., and Menon, R., *Parallel Programming in OpenMP*, Academic Press, San Diego, 2001.

[26]Gropp, W., Lusk, E., and Skjellum, A., *Using MPI: Portable Parallel Programming with the Message-Passing Interface*, The MIT Press, Cambridge, MA, 2nd ed., 1999.

[27]Hung, C. M. and MacCormack, R. W., "Numerical Solutions of Supersonic and Hypersonic Laminar Compression Ramp Flows," *AIAA Journal*, Vol. 14, No. 4, 1976, pp. 475–481.

[28]Power, G. D. and Barber, T. J., "Analysis of Complex Hypersonic Flows with Strong Viscous/Inviscid Interaction," *AIAA Journal*, Vol. 26, No. 7, 1988, pp. 832–840.

[29]Rizzetta, D. and Mach, K., "Comparative Numerical Study of Hypersonic Compression Ramp Flows," AIAA Paper 89-1877, American Institute of Aeronautics and Astronautics, Reston, VA, June 1989.

[30]Rudy, D. H., Thomas, J. L., Kumar, A., Gnoffo, P. A., and Chakravarthy, S. R., "Computation of Laminar Hypersonic Compression-Corner Flows," *AIAA Journal*, Vol. 29, No. 7, 1991, pp. 1108–1113.

[31]Gaitonde, D. and Shang, J. S., "The Performance of Flux-Split Algorithms in High-Speed Viscous Flows," AIAA Paper 92-0186, American Institute of Aeronautics and Astronautics, Reston, VA, January 1992.

[32]Updike, G. A., Shang, J. S., and Gaitonde, D. V., "Hypersonic Separated Flow Control Using Magneto-Aerodynamic Interaction," AIAA Paper 2005-0164, American Institute of Aeronautics and Astronautics, Reston, VA, January 2005.

[33]Edney, B., "Anomalous Heat-Transfer and Pressure Distributions on Blunt Bodies at Hypersonic Speeds in the Presence of an Impinging Shock," FFA Report 116, Aeronautical Research Institute of Sweden, Stockholm, Sweden, February 1968.

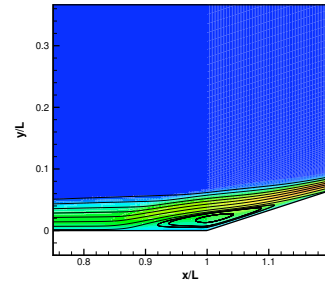American Institute of Aeronautics and Astronautics Paper 2006-1007
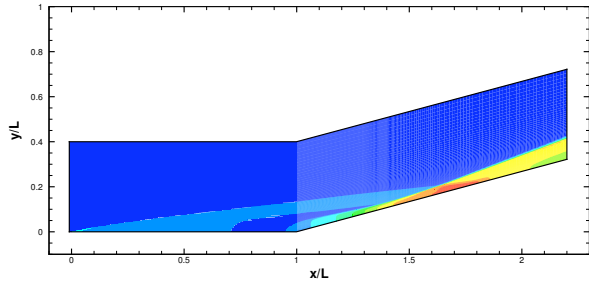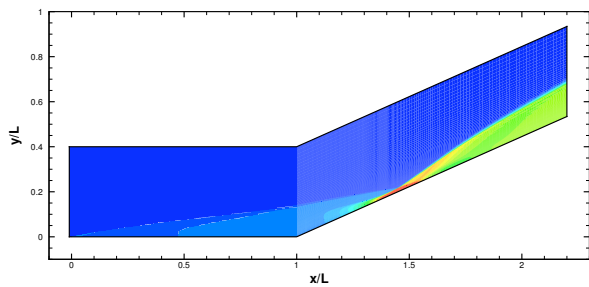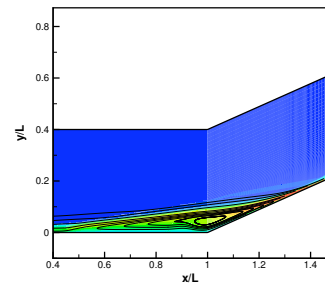
(a) Pressure field, 15° ramp case.
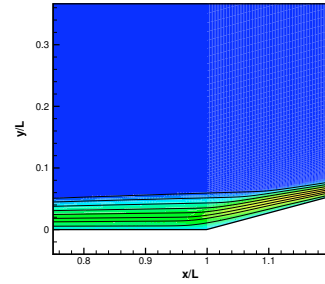
(b) Temperature field and streamlines, 15° ramp case.
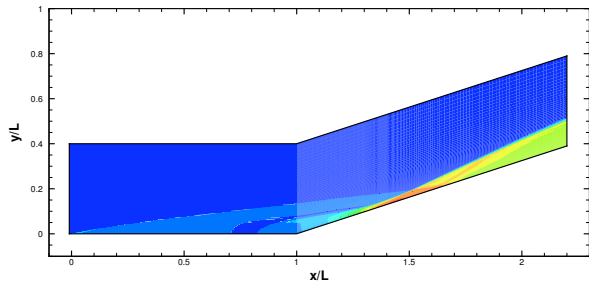
(c) Pressure field, 18° ramp case.
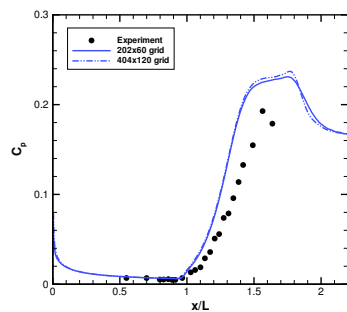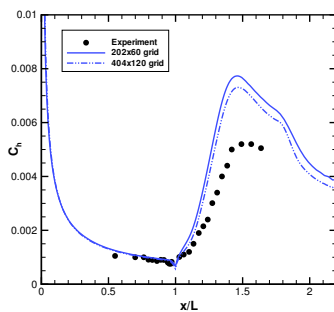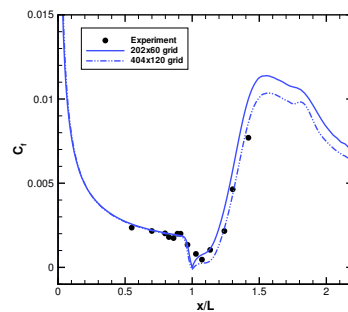

(d) Temperature field and streamlines, 18° ramp case.

(e) Pressure field, 24° ramp case.

(f) Temperature field and streamlines, 24° ramp case.

Figure 1. Flow structure, two-dimensional computations, 404×120 grid.

(a) Pressure coefficient, 15° ramp.

(b) Heat transfer coefficient, 15° ramp.

(c) Skin friction coefficient, 15° ramp.
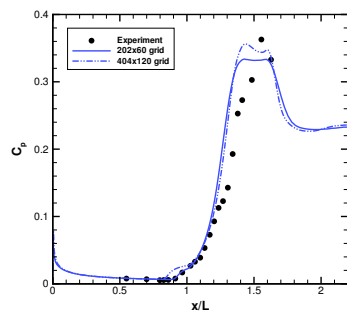
(d) Pressure coefficient, 18° ramp.
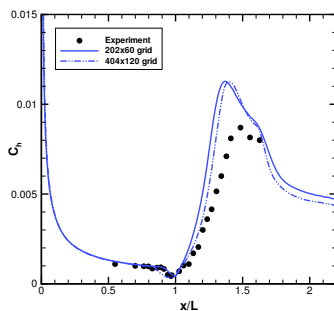
(e) Heat transfer coefficient, 18° ramp.
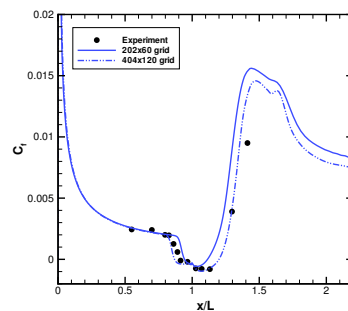
(f) Skin friction coefficient, 18° ramp.
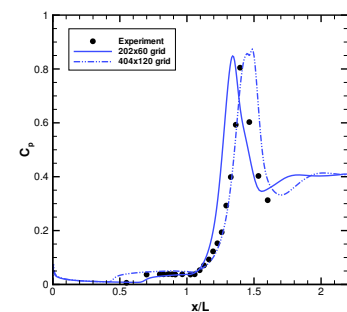
(g) Pressure coefficient, 24° ramp.
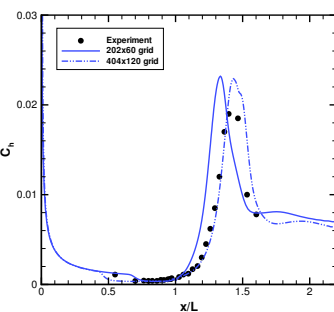
(h) Heat transfer coefficient, 24° ramp.
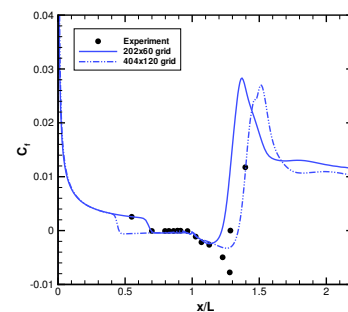
(i) Skin friction coefficient, 24° ramp.

Figure 2. Properties along the wall centerline: experiment and two-dimensional calculations.
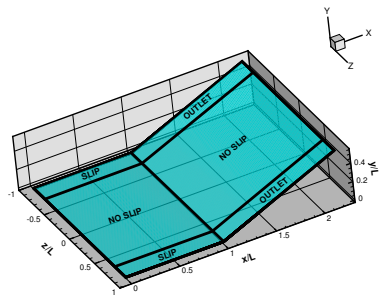
(a) Wall boundary conditions.
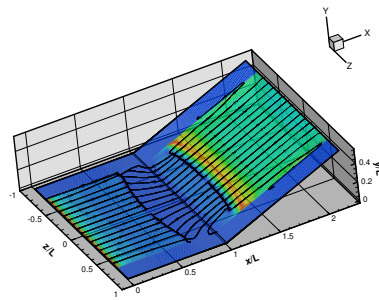
(b) Skin friction.
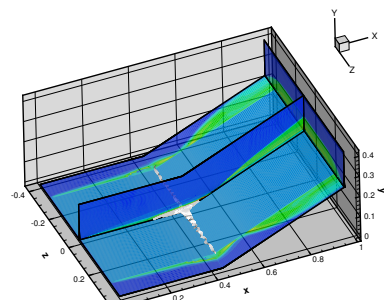
(c) Temperature field.
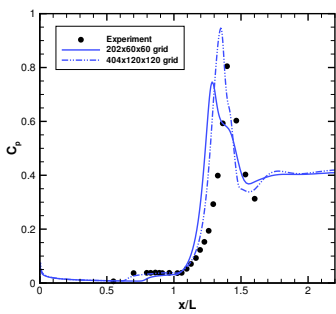
(d) Pressure coefficient on center-line.
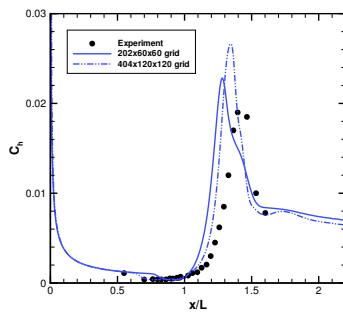
(e) Heat transfer coefficient on cen-terline.
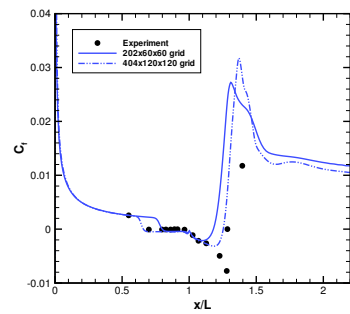
(f) Skin friction coefficient on cen-terline.

Figure 3.   Results of three-dimensional computations of $24°$ ramp flow.
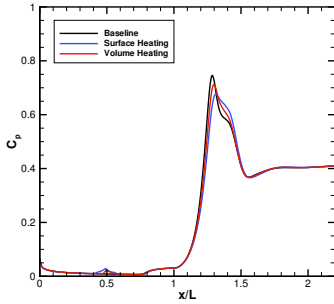
(a) Pressure coefficient.
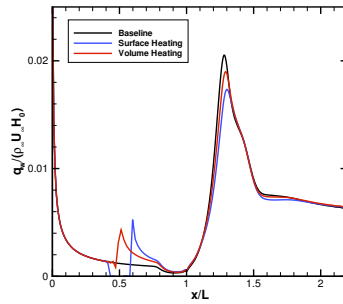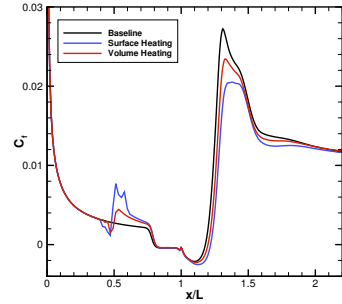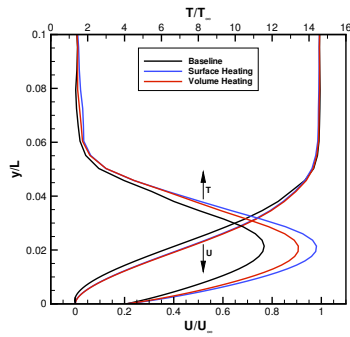
(b) Heat transfer coefficient.

(c) Skin friction coefficient.

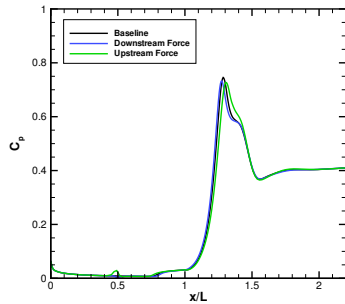(d) Boundary layer profiles at $x/L = 0.81$. Here y is normal and U parallel to the ramp.
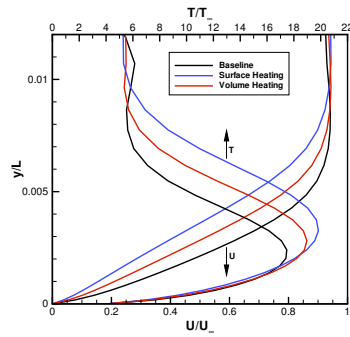
(e) Boundary layer profiles at $x/L = 1.28$. Here y is normal and U parallel to the ramp.
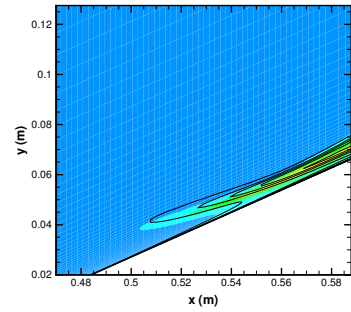
(f) Density distribution near reattachment. Color contours: baseline; black contours: surface heating
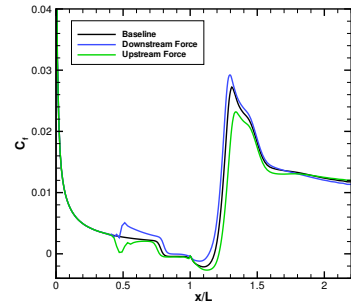
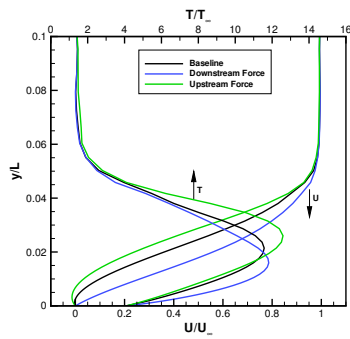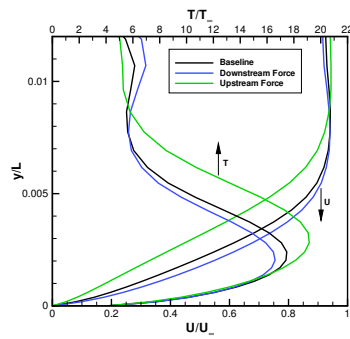Figure 4. Effect of heating on flow structure.

American Institute of Aeronautics and Astronautics Paper 2006-1007
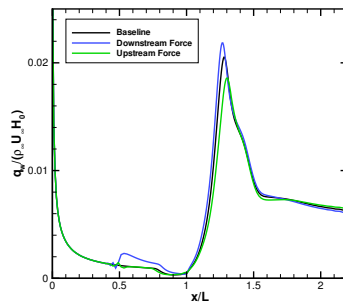
(a) Pressure coefficient.

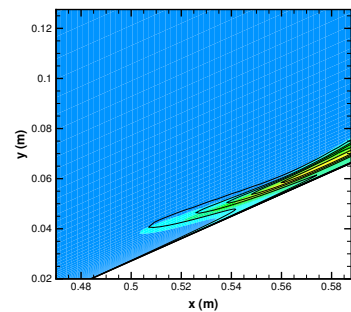(b) Heat transfer coefficient.

(c) Skin friction coefficient.

(d) Boundary layer profiles at $x/L = 0.81$. Here y is normal and U parallel to the ramp.
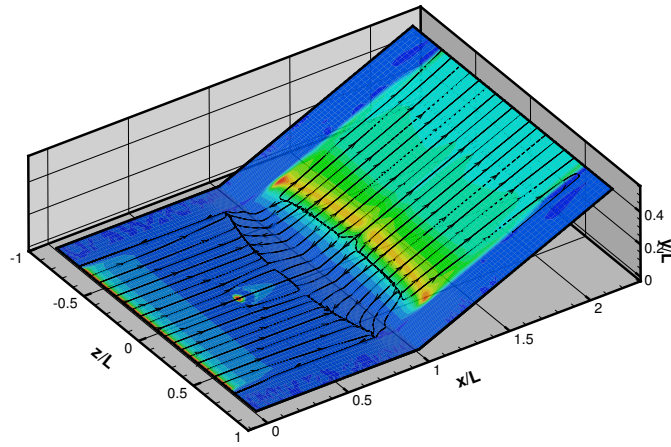
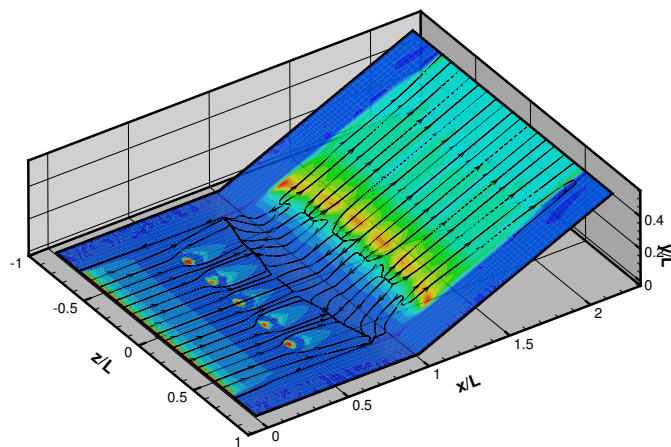(e) Boundary layer profiles at $x/L = 1.28$. Here y is normal and U parallel to the ramp.

(f) Density distribution near reattachment. Color contours: baseline; black contours: upstream body force.

Figure 5. Effect of body forces on centerline properties.

American Institute of Aeronautics and Astronautics Paper 2006-1007

(a) Surface heating.

(b) Surface heating x 5.

Figure 6. Effect of heating on surface streamlines and wall heat transfer distribution.

American Institute of Aeronautics and Astronautics Paper 2006-1007